

# OSPRED: A Coupled Approach to Modeling CME-Driven Space Weather with Automatically-Generated, User-Friendly Outputs

C. Kay<sup>1,2</sup>, M. L. Mays<sup>1</sup>, Y. M. Collado-Vega<sup>1</sup>

<sup>1</sup>Heliophysics Science Division, NASA Goddard Space Flight Center, Greenbelt, MD, USA

<sup>2</sup>Dept. of Physics, The Catholic University of America, Washington DC, USA

## Key Points:

- OSPRED performs ensemble simulations of the Sun-to-Earth behavior of CMEs on time scales relevant for future forecasting
- A standardized set of automatically-generated visualizations can provide essential information for forecasters in an intuitive manner
- Mimicking a forecasting approach, we apply OSPRED to the 22 April 2021 CME to illustrate its capabilities

arXiv:2109.06960v2 [astro-ph.SR] 16 Sep 2021

**Abstract**

Coronal Mass Ejections (CMEs) drive space weather activity at Earth and throughout the solar system. Current CME-related space weather predictions rely on information reconstructed from coronagraphs, sometimes from only a single viewpoint, to drive a simple interplanetary propagation model, which only gives the arrival time or limited additional information. We present the coupling of three established models into OSPREI (Open Solar Physics Rapid Ensemble Information), a new tool that describes Sun-to-Earth CME behavior, including the location, orientation, size, shape, speed, arrival time, and internal thermal and magnetic properties, on the timescale needed for forecasts. First, ForeCAT describes the trajectory that a CME takes through the solar corona. Second, ANTEATR simulates the propagation, including expansion and deformation, of a CME in interplanetary space and determines the evolution of internal properties via conservation laws. Finally, FIDO produces in situ profiles for a CME’s interaction with a synthetic spacecraft. OSPREI includes ensemble modeling by varying each input parameter to probe any uncertainty in their values, yielding probabilities for all outputs. Standardized visualizations are automatically generated, providing easily-accessible, essential information for space weather forecasting. We show OSPREI results for a CME observed in the corona on 2021 April 22 and at Earth on 2021 April 25. We approach this CME as a forecasting proof-of-concept, using information analogous to what would be available in real time rather than fine-tuning input parameters to achieve a best fit for a detailed scientific study. The OSPREI “prediction” shows good agreement with the arrival time and in situ properties.

**Plain Language Summary**

Coronal mass ejections (CMEs) are large plasma structures that erupt from the Sun. These eruptions occur frequently but, depending on their exact properties (such as speed and magnetic field strength and orientation), can have negative effects on human technologies both in space or on the surface of the Earth. It is important to know where a CME is going, when it will arrive, and its properties upon impact. Currently, most CME forecasts are limited to the time of arrival, and potentially the speed at that time, but have little to no additional information. We present OSPREI, which couples existing models to simulate the full Sun-to-Earth evolution of a CME. OSPREI simulates the change in the path of a CME near the Sun, a range of effects during its transit to Earth, and what it would look like as it passes over a spacecraft. OSPREI runs very quickly so we can see how results change as the inputs change. To facilitate forecasts, we have developed a set of standardized figures that present OSPREI results (including CME location, time of arrival, and internal properties) in an easily accessible format displaying the most likely values and the range of possibilities.

**1 Introduction**

Forecasting space weather has gained increased importance in the public eye with recent emphasis from NASA’s Moon to Mars initiative and the US government’s National Space Weather Strategy and Action Plan in 2019 and the Promoting Research and Observations of Space Weather to Improve the Forecasting of Tomorrow (PROSWIFT) Act in 2020. As CMEs are key drivers of space weather, both near the Earth and throughout the rest of the solar system, understanding and forecasting their behavior should be a part of any space weather predictions. Currently, most predictions focus simply on the arrival time of a CME. The severity of CME-driven space weather effects depends on the actual properties of the CME, such as its magnetic field strength and orientation, but currently these are not routinely included in the forecasts.

The first step to determining the potential impact of a CME is to determine where it exists in three-dimensional space. Many eruptions have a visible source on the solar

disk, but some are back-sided or even “stealth” CMEs with no obvious signatures on disk or in the low corona (e.g. Robbrecht et al., 2009; O’Kane et al., 2019). As the CME erupts and begins propagating through the corona it may deflect or rotate, changing its position or orientation from those initial values (e.g. Byrne et al., 2010; Gui et al., 2011). Typically, a CME’s position is reconstructed by visually fitting a geometric shape to one or more coronagraph images (e.g. Xie et al., 2004; Thernisien et al., 2006). This yields information about a CME’s position and size, and potentially its orientation. While relatively easy to routinely apply to observations, there can be significant uncertainties in the reconstructed values (e.g. Mierla et al., 2010). The technique, however, allows for a quick estimate on whether a CME’s path will cause an impact at the Earth or at another location of interest.

Once the trajectory and CME speed, which can be calculated from a height-time profile, are known then the transit time can be determined. At the simplest level this is distance divided by the speed, but most forecasting models incorporated some form of drag with the background solar wind. Analytical models can be as simple as a one-dimensional (e.g. Vršnak & Žic, 2007), or incorporate the geometry and size of the CME (e.g. Žic et al., 2015). More sophisticated models embed a CME pulse in a fluid solar wind background, yielding not only the arrival time but the evolution of the CME itself (e.g. Odstrčil & Pizzo, 1999; Riley et al., 2012; Shiota & Kataoka, 2016; Poedts & Pomoell, 2017). While more computationally expensive than the analytic models, these fluid models can be used for forecasts, but real-time results tend to be restricted to individual runs rather than ensemble studies (see discussion of real-time ensembles in Mays et al. (2015)), limiting any information on the probabilities of specific outcomes. Wold et al. (2018) found a mean absolute error of 10 hours for the real-time forecasts of 273 CMEs from the Community Coordinated Modeling Center using the WSA-ENLIL+Cone model. This value tends to be representative of the error for most current arrival time models (e.g. Riley et al., 2018).

Addressing the severity of the impact requires knowing the CME properties. Most arrival time models also produce the speed of a CME as it is intrinsically related to any physics-based calculation of transit time. The fluid models include predictions of the density of the CME, but typically the CME is treated as a pressure pulse and does not have an internal magnetic structure. Very sophisticated, fully-magnetohydrodynamic simulations are possible (e.g. Török et al., 2018), but most cannot be done in real time. Several analytic models exist that include some evolution of internal CME properties at either coronal or interplanetary distances (Kumar & Rust, 1996; Durand-Manterola et al., 2017; Mishra & Wang, 2018), but these have not yet been incorporated into forecasts.

Alternatively, the magnetic structure of a CME can be forward modeled by combining the observed position of a CME with a flux rope model, allowing for the generation of synthetic in situ profiles (e.g. Kunkel & Chen, 2010; Savani et al., 2015). This method allows for rapid results but does rely on many simplifying assumptions and can only produce the general trends and not any smaller-scale variation. Despite the relative simplicity of this method it is not yet routinely used in forecasts.

Kay and Gopalswamy (2017) and Kay and Gopalswamy (2018) begun working toward a unified Sun-to-Earth CME forecasting model, which led to the Open Solar Physics Rapid Ensemble Information (OSPREDI) model presented in this paper. Kay and Gopalswamy (2017) combined a coronal CME model with an in situ magnetic field model and showed results for 45 CMEs observed by the STEREO spacecraft. Kay and Gopalswamy (2018) showed how ensembles could be used to explore the sensitivity to input parameters for both these models and a simple arrival time model. In Kay and Gopalswamy (2018), the three models functioned independently and were not directly linked. Now, for the first time, we present a fully-coupled suite using the most recent versions of the individual model components and have developed a set of visualizations designed to fa-

facilitate space weather forecasting. We apply OSPREI to an observed CME as if it were being forecast, and describe the resulting “predictions.”

## 2 OSPREI Suite

OSPREI combines three established models into a fully-coupled tool to facilitate potential forecasts. Each of these models has been thoroughly described in their individual papers so here we only provide a brief summary and focus on the flow of information between them. Figure 1 contains a schematic showing the three components of OSPREI, the connections between them, and their individual inputs and outputs, as well as a cartoon of an OSPREI CME.

The first model in the OSPREI chain is Forecasting a CME’s Altered Trajectory (ForeCAT, Kay et al., 2015), which simulates the deflection and rotation of a CME through the corona. ForeCAT relies on a Potential Field Source Surface model (PFSS, e.g. Altschuler & Newkirk, 1969) of the background coronal magnetic field, which we initialize using a synchronic magnetogram corresponding to the date of the eruption. Magnetic tension and pressure gradients from the background cause the CME to deflect in latitude and longitude. Any torque from these forces cause a rotation in the CME’s tilt. The radial velocity profile and expansion of the CME are set using empirical models. Therefore, in ForeCAT, the final coronal speed and size should be treated as inputs rather than outputs like the latitude, longitude, and tilt.

The second component is ANother Type of Ensemble Arrival Time Results (ANTEATR, Kay & Nieves-Chinchilla, 2021), an interplanetary CME model. ANTEATR includes drag, analogous to most other arrival time models, but also includes internal magnetic and thermal forces that determine a CME’s expansion and deformation. The expansion changes both the full angular width and perpendicular angular width ( $AW$  and  $AW_{\perp}$  in Fig. 1, analogous to face-on and edge-on angular widths). The deformation changes the aspect ratio of the CME’s central axis (ratio of  $L_r$  to  $L_{\perp}$  in Fig. 1) and the cross section ( $r_r$  to  $r_{\perp}$ ). Typically, we find that the angular widths remain constant or slowly decrease and that the CME pancakes, or flattens in the radial direction relative to the perpendicular direction. ANTEATR uses the simulated position and orientation from ForeCAT (as well as the input coronal speed and size) and determines the arrival time, as well as the CME propagation and expansion speeds, size, and shape upon arrival. It also provides the internal properties (density, temperature, and magnetic field strength), which evolve according to conservation laws.

The final component is the ForeCAT In situ Data Observer (FIDO, Kay et al., 2017), which creates synthetic in situ profiles. FIDO takes the position and orientation from ForeCAT and the evolved CME properties and arrival time from ANTEATR. FIDO determines the relative position of the spacecraft to the CME and calculates the magnetic field vector and velocity for that specific location. It also estimates the Kp index from the speed and magnetic field as done in Kay et al. (2020). Within FIDO, the CME continues to expand as it passes over the spacecraft according to the speeds provided by ANTEATR. FIDO can also forecast the shock and sheath ahead of a CME using the Rankine-Hugoniot shock conditions with the CME and solar wind properties (Kay et al., 2020). This is a simple analytic shock model for the average sheath and cannot produce the stochastic fluctuations that are commonly observed.

Within OSPREI these components are fully coupled so that a single call to the model runs the full Sun-to-Earth simulation. OSPREI can also be set to run an ensemble where the user specifies the number of individual runs, the input parameters to randomly vary, and their ranges. Standardized data files are created, which can then be immediately processed into user-friendly figures using a separate routine. We also note that combinations of the various components of OSPREI can be run instead of the full set. For example,

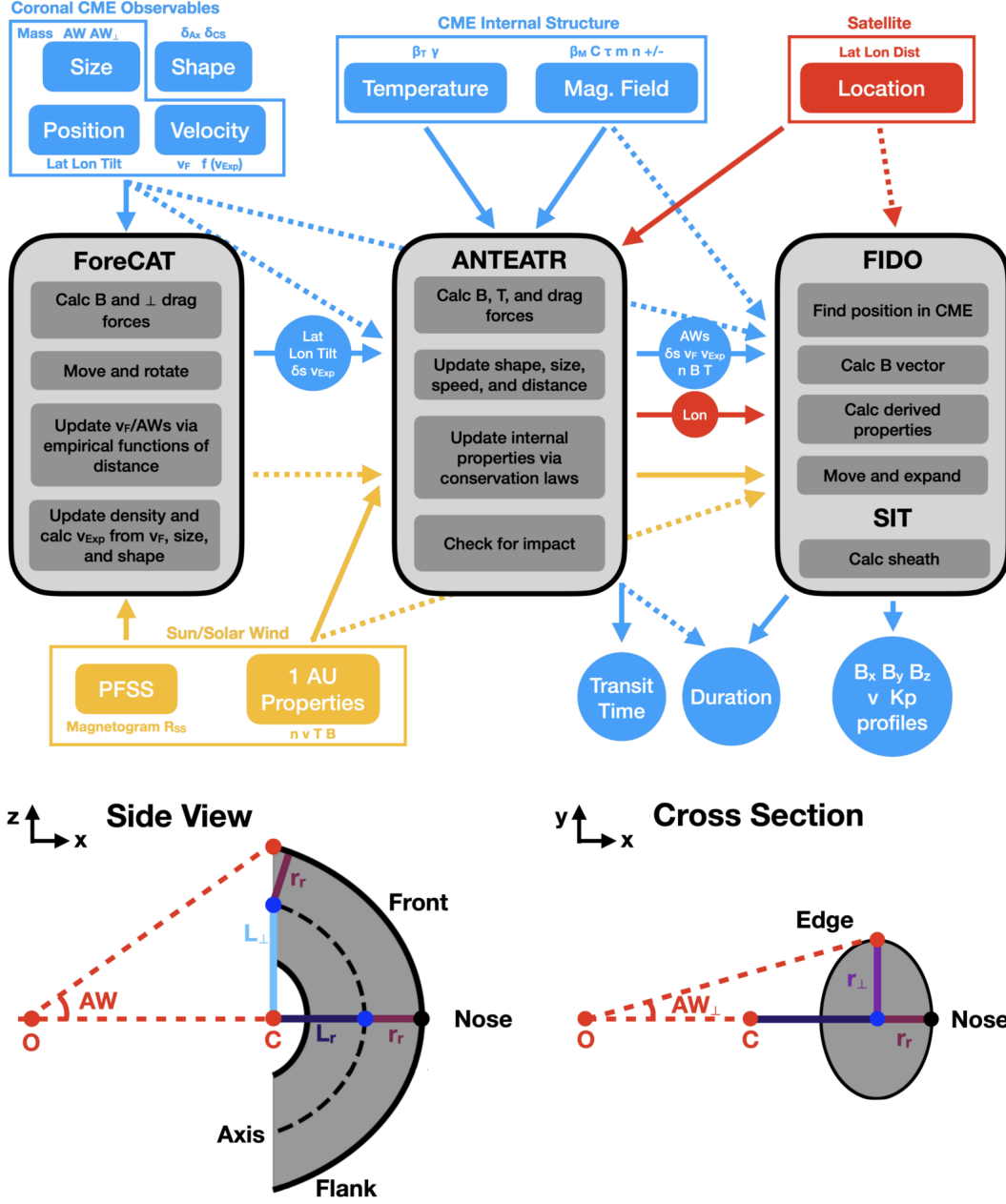


**Figure 1.** Schematic showing the three components of OSPREI and the connections between their inputs and outputs (top). Cartoon showing the CME shape from the side and through the cross section.

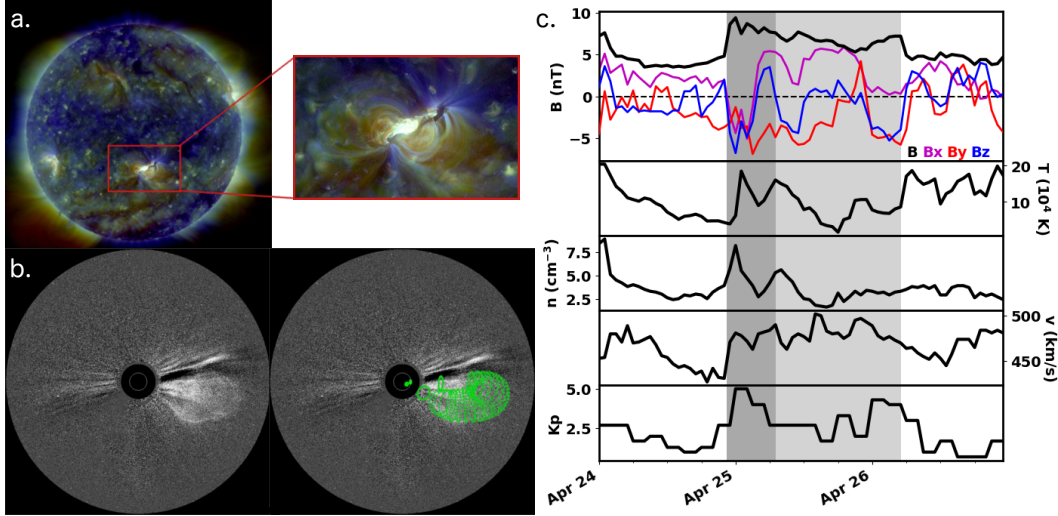


**Figure 2.** (a) Composite EUV image of the solar disk highlighting the CME source region. (b) Coronagraph images of the CME with and without the GCS reconstruction. (c) In situ observations near the time of CME arrival with the sheath (dark gray) and flux rope portions (light gray) highlighted.

one can specify the coronal position and orientation from a coronal reconstruction and use those values to drive ANTEATR and FIDO instead of the ForeCAT simulation. OSPREI has begun the model onboarding process at CCMC so that it will become available for the community to run via runs on request and instant runs.

### 3 Observed CME

To illustrate its capabilities, we apply OSPREI to the 2021 April 22 CME. This CME was chosen for no particular reason other than it is a relatively recent CME that is more dynamic than merely a small blob convecting out with the background solar wind. To mimic the approach that would be used for a real-time prediction we use as much information as possible from the Community Coordinated Modeling Center’s (CCMC’s) Space Weather Database Of Notifications, Knowledge, Information (DONKI), which catalogs the forecast information from the Moon to Mars Space Weather Analysis Office.

DONKI lists this CME as erupting from Active Region 12814 at S24W08 (Stonyhurst longitude) and that the eruption is first visible in STEREO A EUVI 195 Å and SDO AIA 171/193 Å starting at 04:21 UT on April 21. The CME then undergoes a north-eastern deflection and is reconstructed at S13E08 in the corona with a reported speed of 803 km/s and angular width of 30°.

Figure 2 shows observations of the 2021 April 22 CME. Fig. 2(a) shows a composite image of SDO AIA channels (171 Å blue, 193 Å green, and 211 Å red) around 04:47 UT. The red rectangle shows the location of the active region and the post eruption arcades, which we zoom in on in the highlight panel. Fig 2(b) shows an image from STEREO COR2A at 08:23 UT with the right panel including our own Graduated Cylindrical Shell reconstruction (GCS, Thernisien et al., 2006), which has a latitude of -10°, longitude of -1° Stonyhurst, and tilt of 20°.

In DONKI, this CME was predicted to arrive at 17:27 UT on April 24 but was linked to an in situ shock arrival at 22:24 UT on April 24. Fig. 2(c) shows OMNI in situ data



around this time span with the top panel showing magnetic field (black is total  $B$ , purple, red, and blue are  $B_x$ ,  $B_y$ , and  $B_z$  in GSE coordinates), the second panel showing the temperature, the third panel showing the number density, the fourth panel showing the velocity, and the bottom panel showing the Kp index. The shaded region corresponds to our CME boundaries with the dark gray in front designated as the sheath and the light gray the CME (or flux-rope-like component) itself. We set the internal boundary at 07:00 UT on April 25 and the end boundary at 5:00 UT on April 26 based on sharp changes in the in situ measurements. These two boundaries are estimates and one could potentially argue for different values but these regions are only used for illustrative purposes and not any quantitative analysis. To mimic a real time forecast we do not use any in situ information about the CME when setting the initial parameters as it would not be available. We do use the upstream in situ solar wind information, which is used for the interplanetary drag and expansion and the sheath calculation, as our focus is not on forecasting the solar wind itself and OSPREI can be coupled with any model designed for that.

#### 4 OSPREI Inputs

We now address how we determine OSPREI inputs from the information that would be available for a real-time forecast. Table 1 lists all 34 parameters that can be varied for an OSPREI simulation. All three components of OSPREI are fully-determined by these numbers and the PFSS background driven by the synchronic magnetogram. The table shows the parameter name, the value used for our test case, and the source for that value. If a parameter is varied within our ensemble then we also include the range considered. Parameters are grouped by OSPREI component, background solar wind, or satellite properties.

While at first glance this may appear an unwieldy number of parameters to set for predictions, we feel it can be managed and that it is the minimum necessary to describe a CME’s full behavior from the Sun to the Earth. First, we emphasize that this is a completely explicit list of every free parameter that could potentially be changed. For our test case we leave 15 parameters at default values, which would likely be done for actual forecasts. Of the 19 parameters remaining, 4 of them correspond to the location of the Earth or satellite of interest, 3 define the background solar wind properties, and 6 can be reconstructed or estimated from coronal observations (either reported in DONKI or our own GCS fit).

This leaves 6 “difficult” parameters, or ones for which default values are not well-constrained. First is the initial tilt of the CME, which we can visually estimate from EUV imagery and make sure this estimate aligns with any polarity inversion lines in the PFSS model. We also have a measure of the tilt in the corona from our GCS reconstruction and would expect the initial value to be similar unless extreme rotations are observed. Next, the perpendicular angular width of the CME can technically be estimated from the  $\kappa$  parameter in the GCS fit but we find that this parameter is rarely accurately adjusted for scientific reconstructions, let alone real-time predictions, so this is essentially unconstrained beyond what seems like a “reasonable” guess. Similarly, the mass of a CME can be reconstructed from white-light images (e.g. Pluta et al., 2019) but with large uncertainty (Vourlidis et al., 2010; de Koning, 2017) and this is not commonly done for reconstructions. We again pick a reasonable value, assuming mass tends to scale with CME speed and size.

The initial magnetic field strength of the flux rope and internal CME temperature are completely unconstrained. These are two critical parameters for determining the interplanetary behavior and not having a good measure of them for real-time predictions is a major limitation, as it will be for any model sophisticated enough to include forecasts of these internal properties. We hope that continued research will provide a bet-

ter option in the future, such as scaling to flare, active region, or dimming properties (Qiu et al., 2007; Gopalswamy et al., 2017; Dissauer et al., 2019), but for now we pick reasonable values assuming that the scaling parameters tend to increase with CME size/speed. The final uncertain parameter is the handedness of the flux rope. We use the Bothmer-Schwenn relationship, which links the handedness to the hemisphere from which the CME erupts. This relationship is generally true over a large number of CMEs but may not hold for a specific individual CME. Detailed studies can provide a more accurate guess at this handedness (e.g. Palmerio et al., 2017) but may not be feasible on forecasting timescales.

## 5 OSPREI Results

The following subsections show our OSPREI results for the 2021 April 22 CME. We emphasize that our focus is on presenting OSPREI as a tool used in a real-time fashion and the outputs available for predictions, not the details of this specific CME. We have not fine-tuned any parameters to achieve a perfect fit. It is possible that the results could be improved for a detailed scientific study of this event, but our “forecast” approach still yields very encouraging results.

We run an ensemble of 100 members and allow for variations in 15 different initial parameters. The range of the ensemble variations is meant to represent the uncertainty in reconstructed values or our best guesses for plausible values. The full ensemble requires about an hour to run on an average laptop. Any forecasting center would likely have computers with more sophisticated processing power, potentially reducing the run time to tens of minutes.

### 5.1 Coronal Predictions

We begin with the coronal predictions. Figure 3 shows the change in latitude (top panel), longitude (middle), and tilt (bottom) versus distance from ForeCAT. In the left panels, the black line shows the ensemble seed, the dark gray shows the core of the ensemble (one standard deviation about the mean), and the light gray shows the full range. The numbers in the bottom right display the mean and standard deviation for each value at the end of the ForeCAT simulation. The histograms in the right panels show the distribution of the ensemble values at the end of this component.

Fig. 3 shows the expected northeastern deflection for the majority of ensemble members. The CME longitude is shown with respect to the Earth location at the time of the GCS measurement, which is almost  $4^\circ$  lower in Carrington longitude than the start time due to the rotation of the Carrington coordinate system with the solar surface. The majority of CMEs show a slight clockwise rotation, though the full range exhibits more significant rotations in both directions. We typically interpret this spread in rotations as consistent with a background magnetic field causing little to no rotations and that they instead result from slight imbalances in our chosen initial position. The ForeCAT results yield a position and orientation consistent with the DONKI and GCS reconstructions but additionally provide a range of probabilities based on a physics-driven simulation.

### 5.2 Interplanetary Predictions

The next set of figures show results for the ANTEATR interplanetary predictions. Figure 4 shows the evolution of parameters at interplanetary distances, the shading is a similar format to Fig. 3 but all panels include a second parameter in blue. ANTEATR does generate additional results not shown here, such as the speed of the central axis in both the radial and perpendicular directions, but we limit this figure to the values most relevant to provide a clear picture for forecasting. The mean value and standard deviation at the end of the simulation are displayed for each parameter.



**Table 1.** Full List of OSPREI Free Parameters

Parameter	Value	Source
Start time	2021/04/21 22:00	GCS timing
Starting nose height	1.1 $R_s$	Default
<b>ForeCAT CME Properties</b>		
Initial latitude	$-24 \pm 1^\circ$	DONKI
Initial longitude	$260 \pm 1^\circ$	DONKI
Initial tilt	$25 \pm 1^\circ$	EUV estimate
Max coronal velocity	$800 \pm 50$ km/s	DONKI
Max coronal AW	$30 \pm 5^\circ$	DONKI
Max coronal AW $_{\perp}$	$12 \pm 1^\circ$	Unconstrained
Maximum mass	$3 \pm 0.5 \times 10^{15}$ g	Unconstrained
Coronal axis shape $\delta_{Ax}$	$0.75 \pm 0.1$	Default
Coronal cross section shape $\delta_{CS}$	$1 \pm 0.1$	Default
<b>ForeCAT empirical models</b>		
Initial slow rise velocity	50 km/s	Default
Start of rapid acceleration	2.5 $R_s$	GCS timing
Height of max coronal velocity	10 $R_s$	Default
Expansion model AW $_0$	$5^\circ$	Default
Expansion model length scale	1 $R_s$	Default
Height of max mass	10 $R_s$	Default
<b>ANTEATR CME Properties</b>		
Flux rope magnetic scaling	$3 \pm 0.25$	Unconstrained
Elliptical flux rope model [m,n]	[0,1]	Default
Elliptical flux rope model $\tau$	1	Default/Lundquist-like
Elliptical flux rope model $C$	1.927	Default/Lundquist-like
Flux rope temperature scaling	$2 \pm 0.25$	Unconstrained
Adiabatic index $\gamma$	$1.33 \pm 0.1$	Default
Interplanetary expansion factor f	$0.5 \pm 0.1$	Default
<b>FIDO CME Properties</b>		
Flux rope handedness	Right	Bothmer-Schwenn
<b>Solar Wind Properties</b>		
Solar wind 1 AU velocity	$430 \pm 25$ km/s	OMNI
Solar wind 1 AU density	$4 \pm 1$ cm $^{-3}$	OMNI
Solar wind 1 AU magnetic field	$3.5 \pm 1$ nT	OMNI
Solar wind 1 AU temperature	$6.2 \times 10^4$ K	Default
Drag coefficient	1	Default
<b>Satellite Parameters</b>		
Latitude	$-5.033^\circ$	Earth location
Longitude	$258.374^\circ$	Earth location
Distance	213 $R_s$	L1
Orbital Speed	$2.8 \times 10^{-6}$ rad/s	Earth's orbit

All longitudes in Carrington coordinates at the start time.

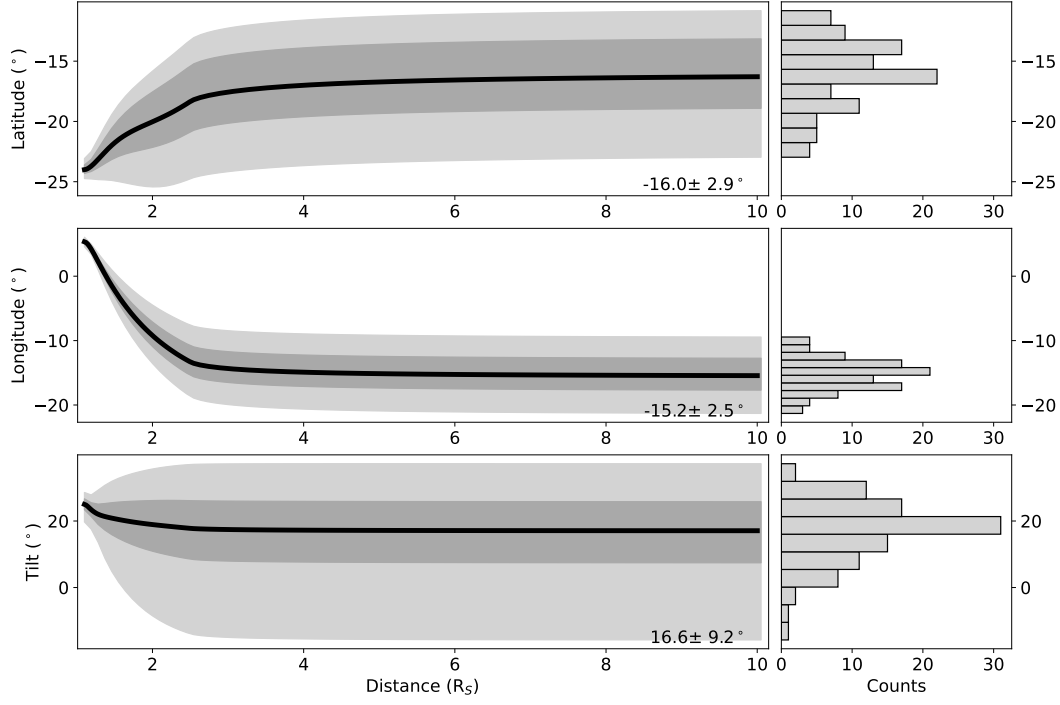


**Figure 3.** ForeCAT results showing the latitude (top), longitude (middle), and orientation (bottom) versus distance. Each panel includes the ensemble seed profile (black), the full range of the ensemble (light gray), and one standard deviation about the mean (dark gray). The histograms on the right show the distribution of the final values for each parameter.

The top left shows the evolution of the angular widths,  $AW$  and  $AW_{\perp}$ . Both widths show a small increase in the first  $20 R_s$  due to the magnetic and thermal forces. Beyond  $50 R_s$ , the ensemble seed shows a slight decrease in both parameters. The full ensemble ranges between slight increases and slight decreases depending on the exact initial parameters but in general is consistent with nearly constant angular widths. The top right shows the change in the axis and cross section aspect ratios,  $\delta_{Ax}$  and  $\delta_{CS}$ . Both decrease, which corresponds to a pancaking effect where the radial direction becomes relatively shortened due to the combined effects of drag and axial magnetic forces. Both ratios show a sharp decrease early on but a continued decrease at farther distances, though a few outliers show a secondary increase in  $\delta_{Ax}$ .

The bottom left panel shows the speed of the CME front,  $v_F$ , and the expansion speed,  $v_{Exp}$ . Technically, we show the rate at which the radial cross section length,  $r_r$  in Fig. 1, increases, but this is analogous to the in situ expansion speed that would be observed for a direct hit at the CME nose.  $v_{Exp}$  shows an initial increase due to an overpressure relative to the background, which causes the increase in  $AW_{\perp}$ , but then decreases as the external pressure becomes larger than that inside.  $v_F$  shows an initial increase, which is driven by the expansion of the cross section pushing the nose forward, but quickly begins decreasing as both the drag and axial magnetic forces act to slow down the forward motion.

The bottom right shows the internal magnetic field strength (taken at the central axis) and the logarithm of the temperature. Both parameters decrease as the CME expands, as expected, but this gives a most probable value and the range for these internal properties upon impact, which is uncommon for a simple analytic prediction.

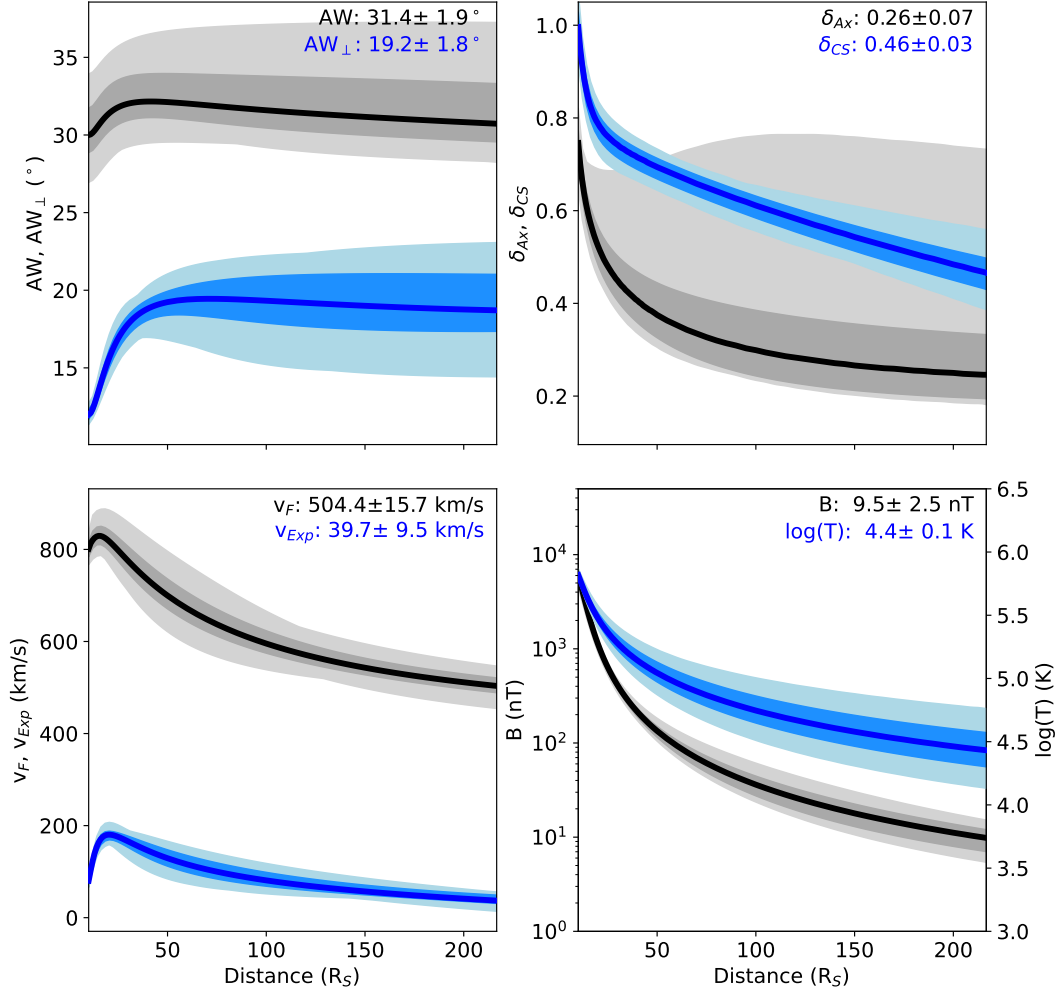


**Figure 4.** Interplanetary evolution of the CME in the same format as Fig. 3. The top left shows the angular width (black) and perpendicular angular width (blue). The top right shows the axial (black) and cross section (blue) aspect ratios. The bottom left shows the front velocity (black) and the expansion velocity (blue). The bottom right shows the magnetic field strength (black) and temperature (blue).

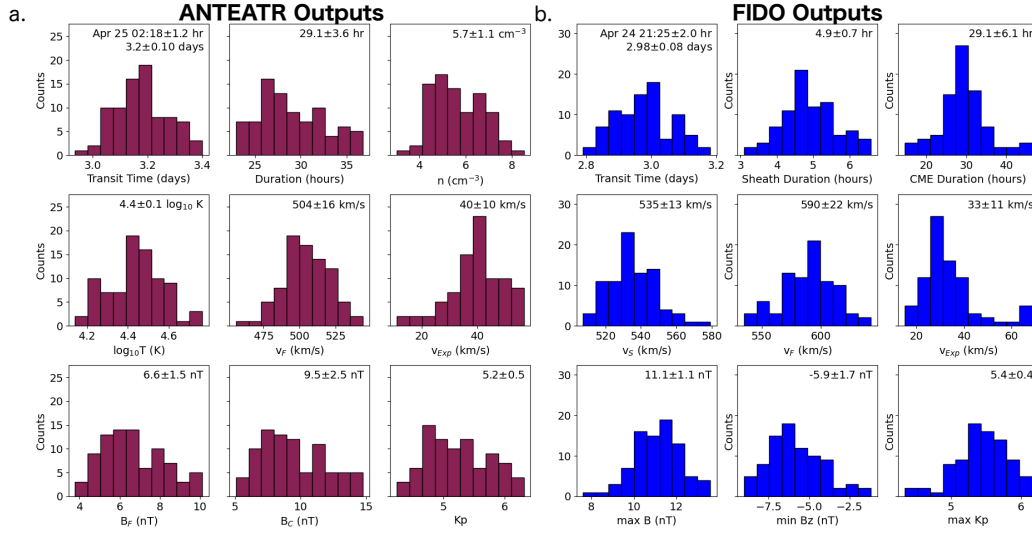


**Figure 5.** Histograms of the outputs from ANTEATR (a) and FIDO (b). Where possible, comparable values between ANTEATR and FIDO are presented in analogous panels (i.e. the front velocity in both center panels).

Instead of looking at full profiles, forecasters may prefer to simply see the range of possibilities at the time of impact. Figure 3(a) shows histograms of different values from ANTEATR. ANTEATR does not simulate the full path of the satellite through the CME, that is only performed in FIDO, so properties such as the duration are estimated from the geometry. The histograms include  $v_F$  and  $v_{Exp}$  as in Fig. 4 and are global properties of the CME rather than what one may observe in situ for that specific impact location. As such, if available, outputs from FIDO (shown in Fig. 5(b)) should be prioritized over analogous ANTEATR outputs.

The top left panel shows the transit time. ANTEATR only simulates the flux rope, the sheath is not included until FIDO, so this corresponds to the arrival of the front of the flux rope. The text displays the mean arrival time of 02:18 on April 25, which is within 5 hours of the boundary we estimated from observations. The top middle panel shows an average duration of 29 hours, which is a bit longer than the observed duration. The top right panel shows an average density of  $5.7 \pm 1.1 \text{ cm}^{-3}$  and the middle left shows a temperature of  $\log(T) = 4.4 \pm 0.1 \text{ K}$ . We find average propagation and expansion speeds of 500 km/s and 40 km/s (middle row, center and right panels), but again, these correspond to the general CME properties, not what may be measured in situ at a specific point of impact. The bottom row shows  $B_F$  (left), the magnetic field at the front of the CME, which is equivalent to the poloidal field at the edge of the cross section, and  $B_C$  (middle), taken at the center of the flux rope and equivalent to the toroidal field at the axis. ANTEATR does not require the handedness of the internal magnetic field so these magnetic field values are unsigned. Finally, we estimate  $Kp$  at the front of the CME using  $v_F$  and  $B_F$ .

### 5.3 In Situ Predictions

The next figures correspond to FIDO results for the synthetic in situ magnetic and velocity profiles. Fig. 5(b) shows histograms of various parameters, analogous to the ANTEATR results in Fig. 5(a) but for a more accurate simulation of the CME-satellite interaction

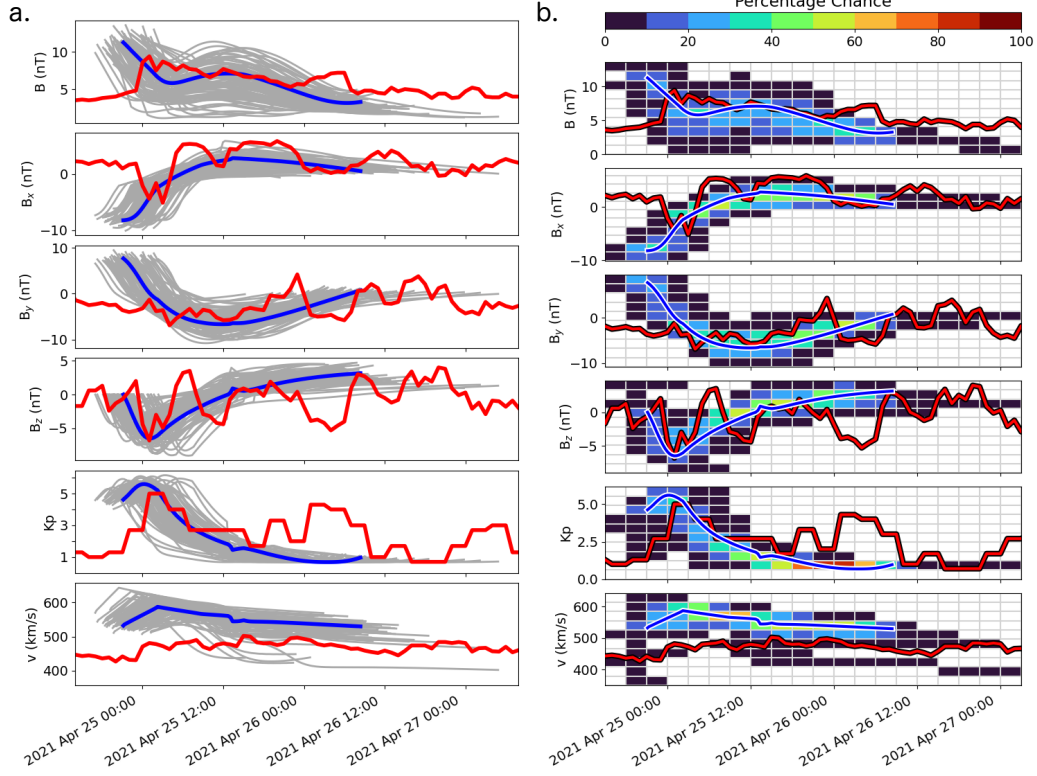


**Figure 6.** (a) Individual in situ profiles for each ensemble member (gray) with the ensemble seed (blue) and OMNI observations (red). (b) Contours of the probability of specific in situ values over time derived from the density of the individual profiles.

and including the CME-driven sheath. Where possible, we include analogous properties in the same location in both figures, but not all panels are directly comparable.

The top row shows the transit time, sheath duration, and CME duration (left to right). The mean CME duration is the same as seen as ANTEATR, suggesting our geometric estimate is fairly accurate, but we do see a slightly larger range from the ensemble members that interact at more oblique angles. The sheath has an average duration of 5 hours and the predicted arrival time is 5 hours earlier than the sheath-free ANTEATR time. The predicted start at 21:25 UT on April 24 is only an hour different than our measured start at 22:24 UT.

The middle row shows the speed in the sheath, at the front of the flux rope, and the expansion speed. The expansion speed is calculated as is done for observations as one half of the difference between the speed at front and end of the flux rope portion. These histograms show a higher front speed (590 km/s) but lower expansion speed (33 km/s) for the in situ values at the actual impact location as compared to the ANTEATR values given for the nose.

The bottom row shows the maximum magnetic field ( $11 \pm 1$  nT) and the most negative  $B_z$  ( $-6 \pm 2$  nT) within each ensemble profile (left and center panels). The bottom right panel shows the maximum Kp, which is largest value calculated over the full profile from the velocity and magnetic field. We find a mean maximum Kp of 5.4 with a stan-

dard deviation of 0.4, which we find occurs in the sheath and is slightly higher than that estimated from ANTEATR alone.

Figure 6 shows the full in situ profiles in two different formats, which provide more details than the histograms, but may not be as easy to quickly interpret. Both panels show the total magnetic field strength ( $B$ ), three components in GSE coordinates ( $B_x$ ,  $B_y$ ,  $B_z$ ), the estimated Kp, and the in situ velocity profiles, from top to bottom. Both panels show the observed in situ profiles in red and the seed profile in blue. Panel (a) shows the individual profiles for each ensemble member (gray line) whereas panel (b) shows the percentage chance for different values of each parameter. The values are weighted by the total number of CMEs that impact the spacecraft so that in many time cells the total percentage of any value is less than 100 as not all CMEs were present at that time.

We see that the majority of the profiles are in general agreement with the observations. The gray lines tend to fall around the red observations, similarly for the brightest contour regions. All ensemble members miss the second increase in Kp around 00:00 UT on April 26, which results from a fluctuation in  $B_z$  not captured by the simple, analytic flux rope model. It may be possible to improve the fit with a different flux rope model but no ensemble members reproduce this bump, though some have profiles that remain negative rather smoothly rotating to positive values. The majority of ensemble members have a in situ velocity 50-100 km/s higher than the observations. This may be improved by changing the interplanetary expansion factor,  $f$ , from its default value. This determines whether the CME is initially expanding self-similarly or convecting with the solar wind before the ANTEATR forces take over. Again, our focus is presenting the OSPREI tool and the outputs that can be generated for forecasts so we leave values at reasonable defaults that would be used in real-time predictions rather than fine-tuning them for a best fit.

These figures show the variety in the ensemble in more detail than the histograms since they show the full profiles instead of reducing time-variations to single values. For example, instead of just having a number for the minimum  $B_z$ , the profiles show that for most cases this value occurs several hours into the passage at the sheath/flux-rope boundary and it is a quick dip into negative  $B_z$ , rather than an extended duration due to the rotation in the flux rope magnetic field. The range in arrival times and durations becomes more obvious. In Fig. 6(a) many of the individual starts and ends of the simulations are visible. In Fig. 6(b) these variation cause there to be a quite long time range where there is a small probability of CME impact. A time range nearly twice as long as the duration of the ensemble seed profile contains nonzero probabilities, though the strong probabilities cover a much smaller range. Fig. 6(a) also shows a few outlier cases that behave differently from the majority of the population. These have very low  $B$  and shorter sheath and flux rope durations. We also see a few very long duration cases with weak magnetic field strength. We will briefly discuss these cases in Section 6.2.

## 6 Further Analysis

### 6.1 Spatial Variations

FIDO yields the full in situ profile for a specific trajectory through the CMEs, but it may be of use to see how things would change if the location of the CME were spatially shifted. We use the CME geometries and internal properties at the time of impact (from ANTEATR) to produce contour maps of various properties, shown in Figure 7. We project the location of each ensemble member onto a flattened map of latitude and longitude relative to the Earth's (or satellite's) location (marked with a pale blue dot).

The top left panel shows the percentage chance of impact. This is simply the sum of CMEs that impact that location divided by the total number of CMEs that reach the satellite distance. The denominator is not necessarily the same as the number in the en-



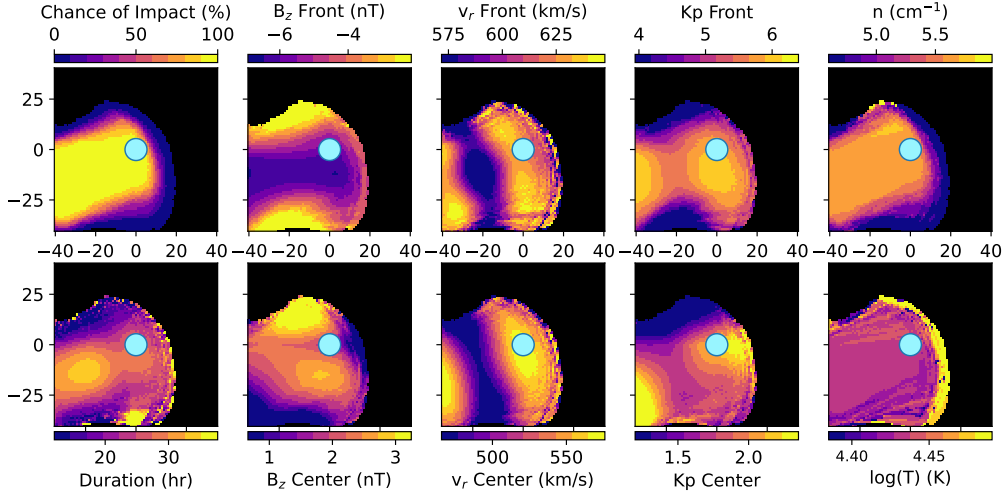


**Figure 7.** Spatial contours of different values using the location and internal properties of the individual ensemble members. The pale blue dot indicates the location of the Earth at the time of impact.

semble, it is possible that the random variations lead to input parameters than make the internal magnetic forces unstable (e.g. combination of low mass with high magnetic field scaling and large  $AW$ ). We do not include these “failed” unstable CMEs in the percentage calculation but we do include the misses that propagate the full distance and do not make contact. For the example CME we find that the impact occurs toward the flank of the CME and we are nearly at the boundary between the core where all CMEs overlap and the region only reached by a few CMEs.

The bottom left panel shows the CME duration using the geometric estimate for the flux rope duration from ANTEATR, rather than a full in situ simulation value including the sheath, as from FIDO. Each location shows the average of all CMEs that impact there. Most of the panel shows the duration decreasing as one moves in latitude towards the edges of the cross section. The variations become more unstructured toward the regions with a low chance of impact (such as at low latitudes) since the average is then determined from a low number of ensemble regions that impact that location.

The middle three panels on both rows show properties at the front and center of the CME (top and bottom respectively). From left to right we show  $B_z$ , the radial velocity  $v_r$ , and the estimated Kp. Both the RTN and GSE coordinate systems depend on the latitude and longitude of the observer. The values we show correspond to rotating these systems to each specific location within the figure, rather than using fixed systems at the position indicated by the pale blue dot. We note that we do include an estimate of the decrease in  $B$  due to CME expansion and flux conservation during the time between the satellite interacting with the front and center of the CME. This CME is right-handed with an axial field pointing toward positive longitude so we see a stronger negative  $B_z$  at the front than in the center. At the front, as one moves in latitude away from the nose  $B_z$  decreases due to the change in the local poloidal direction rather than an actual decrease in the magnitude of the poloidal field. The toroidal field predominantly points in an east-west direction and the little bit of tilt only produces a small positive  $B_z$  near the central axis of the CME, as seen in the bottom panel.

The velocity contours combine the effects of different parts of the axis and cross section expanding at different rates with the local orientation of the radial vector. With a pancaked CME the edges tend to be moving faster but at a more oblique angle to the radial. For the test case, this yields a faster radial velocity near the edges than at the nose. We also consistently find a larger speed at the front than at the center as this case is still expanding at the time of impact.

The Kp contours combine the trends of the  $B_z$  and  $v_r$  panels. At the front we see that the Kp would decrease if the impact moved in longitude toward the nose, which has lower  $v_r$ , and decrease with northern movement in latitude toward regions of more positive  $B_z$ . Near the axis of the CME, the pattern is more complicated due to the individual components being more complicated in the center, but in general the Kp remains below 2.

The right panels show the number density (top) and logarithm of the temperature (bottom). Both of these parameters are treated as uniform within a individual simulation so the spatial variations only result from the the actual spatial distribution of the ensemble CMEs, not any internal structure. We do not see as much variation in these parameters, with the exception of some particularly hot CMEs in the low percentage chance of impact region.

## 6.2 Analyzing Trends

While the previous figures have shown the range of possibilities suggested by the ensemble modeling, they have not provide much, if any, reason for those variations. Figure 8 provides that information for when a forecaster wishes to dive deeper. The horizontal axis shows each of the inputs varied within the ensemble and the vertical axis shows significant outputs that can be quantified by a single number, such as those shown in the histograms. Each panel shows a scatter plot between an input and an output and are colored according to their correlation coefficient to help illuminate any trends. Some trends are expected, such as those between parameters that are both inputs and outputs (e.g. large initial  $AW$  correlated with large final  $AW$ ). Others are less direct but still expected (e.g. higher  $B_{SW}$  leading to higher CME max  $B$  when the  $B$  scaling is constant). In some cases we find that expected trends may be washed out by the model physics (e.g. final  $T$  is only slightly correlated with initial temperature scaling). Other times, unexpected trends may occur (e.g. minimum  $B_z$  with initial latitude or number density with  $B_{SW}$ ).

This figure also helps investigate outliers, such as seen in the in situ figures. We see that for many of the final properties the ensemble members can be separated into two distinct populations, the main group and a smaller group of outliers. This is most visible in the two aspect ratios,  $\delta_{Ax}$  and  $\delta_{CS}$ , both velocities,  $v_F$  and  $v_{Exp}$ , and  $AW_{\perp}$ . The outlier cases all have a less pancaked shape, higher final propagation and expansion velocities, and smaller perpendicular angular width. While we see a clear separation in the final properties, the trends with initial properties, or which specific inputs cause this behavior, are less obvious. These cases tend to have smaller initial  $AW$  and larger  $\delta_{Ax}$ , but are not that dissimilar from the rest of the ensemble. Our interpretation is that the smaller  $AW$  creates a higher CME density and higher  $\delta_{Ax}$  reduces the internal magnetic forces, both of which weaken the pancaking and drag forces. While this level of interpretation may not be necessary for routine forecasting, it is essential to recognize while the majority of the ensemble falls within the main group, making that the most probable forecast, there is a small possibility of the observed behavior mirroring that of this subset instead of the mean values.

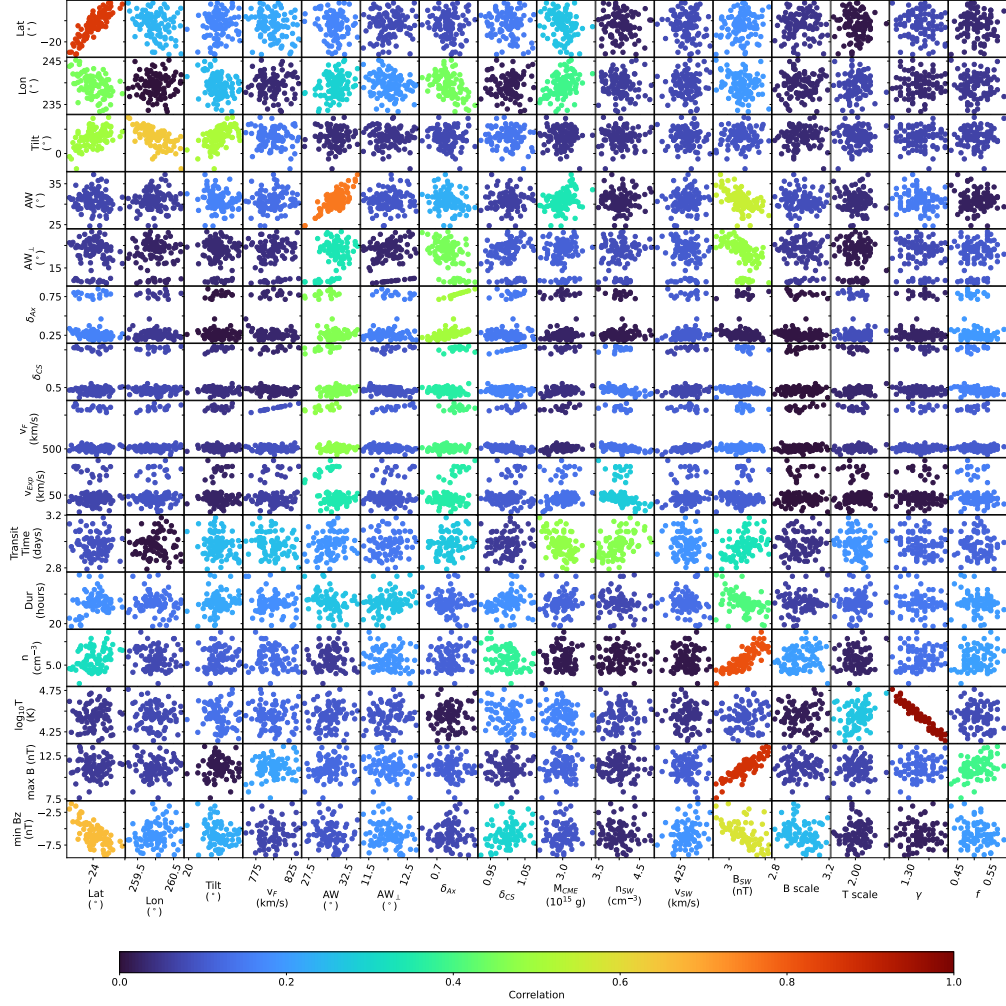


**Figure 8.** Scatter plots showing the relation between variations in input parameters (horizontal axes) and outputs (vertical axes). The data in each panel is colored according to the correlation between that input-output pair.

## 7 Conclusion

We have presented the new CME forecasting suite OSPREI, which represents the combination of previously established models and includes standardized, user-friendly visualizations. To demonstrate OSPREI's capabilities we have applied it to the CME observed in the corona on 2021 April 22. We mimic a forecasting approach, using the best information that would be available in a real-time scenario, rather than fine-tuning inputs to optimize the output for a detailed scientific study. OSPREI simulates the coronal deflection and rotation, the interplanetary expansion, deformation, and arrival time, and the expected in situ profiles, including an estimate of the Kp. From an ensemble of 100 runs we have not only the most probability value for each output but a range of possibilities and their likelihoods. Our visualizations provide this essential information in an easily-accessible format. We also include more complex visualization providing further details on expected spatial variations in the CME properties and digging into the ensemble details by linking the inputs and outputs and illuminating any trends that may be affecting different populations within the ensemble.

## Acknowledgments

CK is supported by the National Aeronautics and Space Administration under Grant 80NSSC19K0274 issued through the Heliophysics Guest Investigators Program and by the National Aeronautics and Space Administration under Grant 80NSSC19K0909 issued through the Heliophysics Early Career Investigators Program.

The full OSPREI code is archived through Zenodo at <https://zenodo.org/badge/latestdoi/236822923> with DOI 10.5281/zenodo.5507441 and is available at GitHub at <https://github.com/ckay314/OSPREI>. The DONKI entry for the 2021 April 22 CME is available at <https://kauai.ccmc.gsfc.nasa.gov/DONKI/view/CME/16772/1> and the shock arrival at <https://kauai.ccmc.gsfc.nasa.gov/DONKI/view/IPS/16784/1>. SDO composite imagery is available from <https://sdo.gsfc.nasa.gov/data/aiahmi/>. The STEREO coronagraph data is available at [https://secchi.nrl.navy.mil/secchi\\_flight/images](https://secchi.nrl.navy.mil/secchi_flight/images). OMNI data are available at <https://omniweb.gsfc.nasa.gov/>.

## References

- Altschuler, M. D., & Newkirk, G. (1969, September). Magnetic Fields and the Structure of the Solar Corona. I: Methods of Calculating Coronal Fields. *Solar Physics*, 9, 131-149. doi: 10.1007/BF00145734
- Byrne, J. P., Maloney, S. A., McAteer, R. T. J., Refojo, J. M., & Gallagher, P. T. (2010, September). Propagation of an Earth-directed coronal mass ejection in three dimensions. *Nature Communications*, 1, 74. doi: 10.1038/ncomms1077
- de Koning, C. A. (2017, July). Lessons Learned from the Three-view Determination of CME Mass. *The Astrophysical Journal*, 844(1), 61. doi: 10.3847/1538-4357/aa7a09
- Dissauer, K., Veronig, A. M., Temmer, M., & Podladchikova, T. (2019, April). Statistics of Coronal Dimmings Associated with Coronal Mass Ejections. II. Relationship between Coronal Dimmings and Their Associated CMEs. *The Astrophysical Journal*, 874(2), 123. doi: 10.3847/1538-4357/ab0962
- Durand-Manterola, H. J., Flandes, A., Rivera, A. L., Lara, A., & Niembro, T. (2017, December). CMEs' Speed, Travel Time, and Temperature: A Thermodynamic Approach. *Journal of Geophysical Research (Space Physics)*, 122(12), 11,845-11,856. doi: 10.1002/2017JA024369
- Gopalswamy, N., Yashiro, S., Akiyama, S., & Xie, H. (2017, April). Estimation of Reconnection Flux Using Post-eruption Arcades and Its Relevance to Magnetic Clouds at 1 AU. *Solar Physics*, 292(4), 65. doi: 10.1007/s11207-017-1080-9
- Gui, B., Shen, C., Wang, Y., Ye, P., Liu, J., Wang, S., & Zhao, X. (2011, July).

- Quantitative Analysis of CME Deflections in the Corona. *Solar Physics*, 271, 111-139. doi: 10.1007/s11207-011-9791-9
- Kay, C., & Gopalswamy, N. (2017, December). Using the Coronal Evolution to Successfully Forward Model CMEs' In Situ Magnetic Profiles. *Journal of Geophysical Research (Space Physics)*, 122(A11), 11. doi: 10.1002/2017JA024541
- Kay, C., & Gopalswamy, N. (2018, Sep). The Effects of Uncertainty in Initial CME Input Parameters on Deflection, Rotation,  $B_z$ , and Arrival Time Predictions. *Journal of Geophysical Research (Space Physics)*, 123(9), 7220-7240. doi: 10.1029/2018JA025780
- Kay, C., Gopalswamy, N., Reinard, A., & Opher, M. (2017, February). Predicting the Magnetic Field of Earth-impacting CMEs. *The Astrophysical Journal*, 835, 117. doi: 10.3847/1538-4357/835/2/117
- Kay, C., & Nieves-Chinchilla, T. (2021, May). Modeling Interplanetary Expansion and Deformation of CMEs With ANTEATR PARADE: 1. Relative Contribution of Different Forces. *Journal of Geophysical Research (Space Physics)*, 126(5), e28911. doi: 10.1029/2020JA028911
- Kay, C., Nieves-Chinchilla, T., & Jian, L. K. (2020, February). FIDO-SIT: The First Forward Model for the In Situ Magnetic Field of CME-Driven Sheaths. *Journal of Geophysical Research (Space Physics)*, 125(2), e27423. doi: 10.1029/2019JA027423
- Kay, C., Opher, M., & Evans, R. M. (2015, June). Global Trends of CME Deflections Based on CME and Solar Parameters. *The Astrophysical Journal*, 805, 168. doi: 10.1088/0004-637X/805/2/168
- Kumar, A., & Rust, D. M. (1996, July). Interplanetary magnetic clouds, helicity conservation, and current-core flux-ropes. *Journal of Geophysical Research*, 101(A7), 15667-15684. doi: 10.1029/96JA00544
- Kunkel, V., & Chen, J. (2010, June). Evolution of a Coronal Mass Ejection and its Magnetic Field in Interplanetary Space. *The Astrophysical Journal Letters*, 715, L80-L83. doi: 10.1088/2041-8205/715/2/L80
- Mays, M. L., Taktakishvili, A., Pulkkinen, A., MacNeice, P. J., Rastätter, L., Odstrčil, D., ... Kuznetsova, M. M. (2015, June). Ensemble Modeling of CMEs Using the WSA-ENLIL+Cone Model. *Solar Physics*, 290, 1775-1814. doi: 10.1007/s11207-015-0692-1
- Mierla, M., Inhester, B., Antunes, A., Boursier, Y., Byrne, J. P., Colaninno, R., ... Zhukov, A. N. (2010, January). On the 3-D reconstruction of Coronal Mass Ejections using coronagraph data. *Annales Geophysicae*, 28, 203-215. doi: 10.5194/angeo-28-203-2010
- Mishra, W., & Wang, Y. (2018, September). Modeling the Thermodynamic Evolution of Coronal Mass Ejections Using Their Kinematics. *The Astrophysical Journal*, 865(1), 50. doi: 10.3847/1538-4357/aadb9b
- Odstrčil, D., & Pizzo, V. J. (1999, January). Three-dimensional propagation of CMEs in a structured solar wind flow: 1. CME launched within the streamer belt. *Journal of Geophysical Research*, 104, 483-492. doi: 10.1029/1998JA900019
- O'Kane, J., Green, L., Long, D. M., & Reid, H. (2019, September). Stealth Coronal Mass Ejections from Active Regions. *The Astrophysical Journal*, 882(2), 85. doi: 10.3847/1538-4357/ab371b
- Palmerio, E., Kilpua, E. K. J., James, A. W., Green, L. M., Pomoell, J., Isavnin, A., & Valori, G. (2017, February). Determining the Intrinsic CME Flux Rope Type Using Remote-sensing Solar Disk Observations. *Solar Physics*, 292, 39. doi: 10.1007/s11207-017-1063-x
- Pluta, A., Mrotzek, N., Vourlidis, A., Bothmer, V., & Savani, N. (2019, March). Combined geometrical modelling and white-light mass determination of coronal mass ejections. *Astronomy & Astrophysics*, 623, A139. doi: 10.1051/0004-6361/201833829



- Poedts, S., & Pomoell, J. (2017, April). EUHFORIA: a solar wind and CME evolution model. In *Egu general assembly conference abstracts* (Vol. 19, p. 7396).
- Qiu, J., Hu, Q., Howard, T. A., & Yurchyshyn, V. B. (2007, April). On the Magnetic Flux Budget in Low-Corona Magnetic Reconnection and Interplanetary Coronal Mass Ejections. *The Astrophysical Journal*, 659(1), 758-772. doi: 10.1086/512060
- Riley, P., Linker, J. A., Lionello, R., & Mikic, Z. (2012, July). Corotating interaction regions during the recent solar minimum: The power and limitations of global MHD modeling. *Journal of Atmospheric and Solar-Terrestrial Physics*, 83, 1-10. doi: 10.1016/j.jastp.2011.12.013
- Riley, P., Mays, M. L., Andries, J., Amerstorfer, T., Biesecker, D., Delouille, V., ... Zhao, X. (2018, Sep). Forecasting the Arrival Time of Coronal Mass Ejections: Analysis of the CCMC CME Scoreboard. *Space Weather*, 16(9), 1245-1260. doi: 10.1029/2018SW001962
- Robbrecht, E., Patsourakos, S., & Vourlidas, A. (2009, August). No Trace Left Behind: STEREO Observation of a Coronal Mass Ejection Without Low Coronal Signatures. *The Astrophysical Journal*, 701(1), 283-291. doi: 10.1088/0004-637X/701/1/283
- Savani, N. P., Vourlidas, A., Szabo, A., Mays, M. L., Richardson, I. G., Thompson, B. J., ... Nieves-Chinchilla, T. (2015, June). Predicting the magnetic vectors within coronal mass ejections arriving at Earth: 1. Initial architecture. *Space Weather*, 13, 374-385. doi: 10.1002/2015SW001171
- Shiota, D., & Kataoka, R. (2016, February). Magnetohydrodynamic simulation of interplanetary propagation of multiple coronal mass ejections with internal magnetic flux rope (SUSANOO-CME). *Space Weather*, 14, 56-75. doi: 10.1002/2015SW001308
- Thernisien, A. F. R., Howard, R. A., & Vourlidas, A. (2006, November). Modeling of Flux Rope Coronal Mass Ejections. *The Astrophysical Journal*, 652, 763-773. doi: 10.1086/508254
- Török, T., Downs, C., Linker, J. A., Lionello, R., Titov, V. S., Mikić, Z., ... Wiyaya, J. (2018, mar). Sun-to-earth MHD simulation of the 2000 july 14 “bastille day” eruption. *The Astrophysical Journal*, 856(1), 75. Retrieved from <https://doi.org/10.3847/1538-4357/aab36d> doi: 10.3847/1538-4357/aab36d
- Žic, T., Vršnak, B., & Temmer, M. (2015, June). Heliospheric Propagation of Coronal Mass Ejections: Drag-based Model Fitting. *The Astrophysical Journals*, 218, 32. doi: 10.1088/0067-0049/218/2/32
- Vourlidas, A., Howard, R. A., Esfandiari, E., Patsourakos, S., Yashiro, S., & Michalek, G. (2010, October). Comprehensive Analysis of Coronal Mass Ejection Mass and Energy Properties Over a Full Solar Cycle. *The Astrophysical Journal*, 722, 1522-1538. doi: 10.1088/0004-637X/722/2/1522
- Vršnak, B., & Žic, T. (2007, September). Transit times of interplanetary coronal mass ejections and the solar wind speed. *Astronomy and Astrophysics*, 472, 937-943. doi: 10.1051/0004-6361:20077499
- Wold, A. M., Mays, M. L., Taktakishvili, A., Jian, L. K., Odstreil, D., & MacNeice, P. (2018, March). Verification of real-time WSA-ENLIL+Cone simulations of CME arrival-time at the CCMC from 2010 to 2016. *Journal of Space Weather and Space Climate*, 8(27), A17. doi: 10.1051/swsc/2018005
- Xie, H., Ofman, L., & Lawrence, G. (2004, March). Cone model for halo CMEs: Application to space weather forecasting. *Journal of Geophysical Research (Space Physics)*, 109, 3109. doi: 10.1029/2003JA010226